PCCP

ROYAL SOCIETY OF CHEMISTRY

PAPER

Check for updates

Cite this: *Phys. Chem. Chem. Phys.*, 2020, **22**, 13808

C–F and C–H bond cleavage mechanisms of trifluoromethane ions in low-lying electronic states: threshold photoelectron–photoion coincidence imaging and theoretical investigations

Yan Chen, [ab] Tongpo Yu,[b] Xiangkun Wu,[b] Xiaoguo Zhou, *[b] Shilin Liu, [b] Fuyi Liu[c] and Xinhua Dai*[a]

Received 2nd April 2020,
Accepted 28th May 2020

DOI: 10.1039/d0cp01793k

rsc.li/pccp

Dissociative ionization of trifluoromethane (CHF_3) is investigated in the 13.9–18.0 eV energy range using the threshold photoelectron–photoion coincidence (TPEPICO) technique coupled to a vacuum ultraviolet synchrotron radiation source. Four electronic states of CHF_3^+, *i.e.*, the X^2A_1, A^2A_2, B^2E, and C^2E states, are populated upon ionization. In this energy range, the parent CHF_3^+ ions fully dissociate. For the CHF_3^+ ions in the ground state, the analysis of the time-of-flight profile of the unique CF_3^+ fragment ions suggests statistical dissociation. For the electronically excited CHF_3^+ ions, the C–F bond cleavage preferentially occurs to predominantly produce CHF_2^+ + F. Moreover, all TPEPICO images of the CHF_2^+ ions exhibit identical patterns, with a weak central spot revealing a previously unobserved statistical decomposition pathway, and the predominant ring in the images documents a fast nonstatistical dissociation channel. The unimolecular decomposition mechanisms of the CHF_3^+ ions are illuminated with the aid of the one-dimensional potential energy curves along the C–H and C–F coordinates calculated using the time-dependent density-functional theory. Moreover, a comparison of the dissociation dynamics of CHF_3^+ in these low-lying states with those of CF_3Cl^+ strongly suggests a substituent effect of chlorine atoms on the binding structure.

1. Introduction

Trifluoromethane (CHF_3) is a greenhouse gas with a relatively high atmospheric abundance (22 ppt), global lifetime (222 years), and stratospheric lifetime (2347 years).[1] It is also widely applied in highly selective reactive-ion etching of silicides in the semiconductor industry.[2–4] CHF_3 is considered an ideal clean alternative to Freon or other chlorobromides owing to the absence of chlorine and bromine atoms, which can catalyze the destruction of ozone with high efficiency.[5] The application of CHF_3 in plasma technology[2,4] requires an in-depth understanding of its properties under electron (or ion) impact and photoexcitation with ionizing photons. In particular, accurate energetics (*e.g.*, ionization energies (IEs) and appearance energies (AEs) of the fragments), branching ratios of feasible and competitive dissociation pathways, and the internal energy distributions of the fragments are required. These data are also required for correctly modeling the physics and chemistry of these media.

The molecular geometries and properties of neutral and ionized CHF_3 and related species have been extensively studied using various theoretical and experimental approaches such as the Gaussian-3X (G3X) level or density-functional theory (DFT)-based techniques;[6,7] photoelectron,[8,9] absorption,[10] and fluorescence emission spectroscopy;[11] electron-impact[12–15] and Penning ionizations;[16] and collision-induced dissociation.[17] In particular, many experimental approaches, such as He-I and He-II photoelectron spectroscopy,[8,18] threshold photoelectron–photoion coincidence (TPEPICO) mass spectrometry,[19] and electron-impact ionization[21–24] have been applied to investigate the dissociative photoionization (DPI) of CHF_3. The electronic configurations of these ionized species, IEs, AEs of the fragments, and collision cross sections were determined.

A neutral CHF_3 molecule has C_{3v} symmetry. Its electronic configuration is $[core](4a_1)^2(5a_1)^2(3e)^4(4e)^4(5e)^4(1a_2)^2(6a_1)^2$. The highest occupied molecular orbital (HOMO) ($6a_1$) is dominantly localized on the σ_{C-H} bond, whereas the $1a_2$, 5e, and 4e orbitals are essentially 2pπ orbitals of F atoms. The deeper 3e, $5a_1$, and $4a_1$ orbitals correspond to σ_{C-F}, a mixture of σ_{C-H} and σ_{C-F}, and σ_{C-H} orbitals, respectively.[8] By removing an electron from the

[a] *National Institute of Metrology, Beijing 100013, China. E-mail: daixh@nim.ac.cn*
[b] *Hefei National Laboratory for Physical Sciences at the Microscale, Department of Chemical Physics, University of Science and Technology of China, Hefei 230026, China. E-mail: xzhou@ustc.edu.cn*
[c] *National Synchrotron Radiation Laboratory, University of Science and Technology of China, Hefei 230029, China*

This journal is © the Owner Societies 2020

outermost orbitals, the X^2A_1, A^2A_2, B^2E, and C^2E low-lying electronic states of the CHF_3^+ ion can be populated. The corresponding adiabatic (AIE) and vertical (VIE) IE values have already been measured.[6–8,18,19]

Similar to CF_4,[20] no parent CHF_3^+ ions were observed upon the single-photon ionization of the neutral $CHF_3(X^1A_1)$ in previous experiments.[19,21–24] This indicates the fully dissociative characteristics of CHF_3^+ ions in the Franck–Condon (FC) region. For the dissociation of CHF_3^+ ions in low-lying electronic states (X^2A_1, A^2A_2, B^2E, and C^2E), both CF_3^+ and CHF_2^+ fragment ions were observed owing to the breaking of C–H and C–F bonds, respectively, while ionic fragments resulting from more than one single-bond rupture were not detected at low internal energies. The corresponding AEs were determined to be $AE_{0K}(CF_3^+/CHF_3)$ = 14.14,[8] 13.9,[21] and 13.85 eV[19] and $AE_{0K}(CHF_2^+/CHF_3)$ = 15.7[21] and 15.03[19] eV. In addition, using the formation enthalpies in the active thermochemical tables (ATcT),[25] *i.e.*, $\Delta_fH_{0K}(CHF_3)$ = -688.92 ± 0.43 kJ mol^{-1}, $\Delta_fH_{0K}(H) = 216.034 \pm 0.000$ kJ mol^{-1}, $\Delta_fH_{0K}(CF_3^+) = 409.29 \pm 0.48$ kJ mol^{-1}, and $\Delta_fH_{0K}(F) = 77.255 \pm 0.048$ kJ mol^{-1}, together with the reported $\Delta_fH_{0K}(CHF_2^+)$ of 601.6 ± 2.7 kJ mol^{-1},[26] the reaction enthalpies of two DPI pathways were evaluated to be $\Delta_rH_{0K}(CHF_3 \rightarrow H + CF_3^+ + e) = 13.62 \pm 0.01$ eV and $\Delta_rH_{0K}(CHF_3 \rightarrow F + CHF_2^+ + e) = 14.18 \pm 0.02$ eV, respectively. The higher value of AE_{0K} than that of the corresponding Δ_rH_{0K} implies the a priori existence of a barrier along the respective bond breaking within CHF_3^+. Similar findings were reported after the G3X calculations by He *et al.*[6] Nevertheless, an alternative conclusion was derived by Parkes *et al.*,[19] who performed synchrotron vacuum ultraviolet (VUV) photoionization of CHF_3 in the 13.5–24.5 eV photon energy range using TPEPICO. They recorded the TPEPICO mass spectra of the fragment ions, *i.e.*, CF_3^+, CHF_2^+, and CF^+, and deduced their mean kinetic energy released distributions (KERDs) by fitting the time-of-flight (TOF) profiles of the coincident fragment ions. As the KERDs were close to the impulsive limits and far from statistical dissociation, non-statistical cleavages of the C–H bonds in $CHF_3^+(X^2A_1)$ ions and the C–F bonds in $CHF_3^+(B^2E$ and $C^2E)$ ions were suggested. The non-statistical behaviors generally refer to direct dissociation without barriers, which is not consistent with conclusions based on thermodynamics.[6,21] In addition, the TOF fitting method is inexact owing to an unverified assumption of the isotropic angular distribution of dissociation at each discrete released energy. In fact, it is not obvious how the discrepancy can be clarified without a close examination of the potential energy surfaces of the cationic states along the dissociation coordinates. Therefore, the main motivation behind the present combined theoretical and experimental work is to reinvestigate the DPI of CHF_3. Accordingly, we mapped the potential energy curves of the low-lying electronic states of the CHF_3^+ ions and measured (with a higher resolution) the released kinetic energy and angular distributions of the fragments formed upon the decomposition of the CHF_3^+ parent ion.

In recent decades, the coupling of the TPEPICO ion-imaging technique with synchrotron VUV photoionization[27–29] has become one of the most powerful experimental approaches for studying the dissociation dynamics of internal-energy-selected ions.[30–32] The AEs of the fragments and the branching ratios for each dissociation channel can be determined from the coincidence mass spectra.[33,34] Moreover, the dissociation mechanisms of the state-selected ions can be deduced from the measured KERDs and angular distributions of the fragment ions through theoretical calculations.[20,35–41] As a representative example, the DPI of CF_3Cl has recently been investigated in this way.[39,40] The dissociation mechanisms of two competing fragmentation pathways along the breakages of the C–Cl and C–F bonds were clarified using the TPEPICO ion-imaging results complemented by potential energy curves calculated by density-functional theory (DFT). Compared with CF_3Cl^+, CHF_3^+ ions have identical symmetries and comparable valence-bond electronic-orbital configurations. Thus, the X^2A_1, A^2A_2, B^2E, and C^2E states of CHF_3^+ are expected to exhibit properties similar to those of the A^2A_1, B^2A_2, C^2E, and D^2E states, respectively, of CF_3Cl^+, while the excluded X^2E state of CF_3Cl^+ is essentially formed by removing an electron from the HOMO, which is mainly a σ_{C-Cl} orbital.

In this work, the VUV DPI of CHF_3 was studied through a joint investigation by TPEPICO measurement and theoretical calculations. Following the decomposition of the CHF_3^+ ions in a specific electronic state, the KERDs and angular distributions of the major fragment ions were obtained from their images. For the isovalent CF_3Cl^+ ion, some of the present authors have recently shown that the A^2A_1 and B^2A_2 states play the most important role in its dissociation,[39,40] irrespective of whether the C–F and C–Cl bonds are broken. Similarly, the corresponding X^2A_1 and A^2A_2 states of CHF_3^+ may play key roles in causing C–F and C–H bond cleavages, which will shed light on the present investigation of the DPI of CHF_3. However, to the best of our knowledge, there has been no theoretical study of CHF_3^+ ions in low-excitation states. Therefore, we calculated the adiabatic potential energy curves of CHF_3^+ in the X^2A_1 and A^2A_2 states along the C–H and C–F coordinates to elucidate the unimolecular decomposition of CHF_3^+ ions. Additionally, a comparison of the DPI processes of CHF_3 and CF_3Cl will provide useful information, leading to an in-depth understanding of the effect of substitution of a chlorine atom with a hydrogen atom on the binding structure.

2. Experimental and computational methodologies

All experiments were performed at the BL09U beamline of the National Synchrotron Radiation Laboratory, Hefei, China. The TPEPICO velocity-imaging spectrometer and the details of the beamline have been described previously.[27] The VUV photons from the undulator of an 800 MeV electron-storage ring were dispersed using a 6 m-long monochromator (370 grooves per mm) with an energy-resolving power ($E/\Delta E$) of $\sim$2000 at 15 eV. A gas filter filled with neon was placed in front of the TPEPICO chamber to eliminate higher-order harmonic radiation. The absolute photon energy was calibrated using the well-known ionization energy of argon (15.763 eV),[27] and the TPE energy resolution was better than 10 meV. The photon flux was measured using a silicon photodiode.

A mixture of CHF_3 and helium gases (1 : 10 v/v) with a stagnation pressure of 1.2×10^5 Pa was introduced into the TPEPICO chamber through a 30 μm-diameter nozzle. After being collimated by a 0.5 mm-diameter skimmer, the molecular beam intersected with the VUV beam 10 cm downstream. Under the action of a DC electric field of $\sim$15 V cm^{-1}, photoelectrons and photoions were simultaneously extracted and collected in opposite directions. Along the electron flight path, a repelling field could magnify and map the velocity images; moreover, a mask with a 1.0 mm-diameter hole and a concentric circle in front of the electron detector further subtracted the energetic electron contamination when collecting threshold electrons.[42] To precisely assess the residual ratio of energetic electrons in the threshold photoelectron spectra (TPES), the Rydberg states of argon were chosen to record the photoionization spectrum and TPES.[27] Electrons with energies of $\sim$50 meV were suppressed to approximately 2% in our TPES.[27] Consequently, the collection efficiency and energy resolution of the threshold electrons were significantly improved.[27] A single-start multiple-stop data-acquisition mode[43] was designed to perform coincident measurements, with the photoelectrons collected by the electron detector being used to trigger the TOF measurements of ions. Furthermore, the coincident ions were directly projected onto multichannel plates backed by a phosphor screen (Burle Industries, P43), and the corresponding images were recorded using a thermoelectric-cooling charge-coupled device camera (Andor, DU934N-BV). With a representative extraction electric field of 14 V cm^{-1}, the fragment ion TOF peak was usually broadened to more than 500 ns at full width. Thus, when a pulsed high voltage of $\sim$40 ns was applied to the MCP front surface of the ion detector as a mass gate for a specific fragment ion, the three-dimensional time-sliced velocity map image of the ion was easily recorded. The kinetic energy resolution of our TPEPICO images was better than 3% of $\Delta E/E$.[27]

The geometries of a neutral CHF_3 molecule and its ions and fragments in their respective electronic ground states were optimized at the (U)B3LYP/6-311+G(d,p) level, as implemented in the Gaussian 16 program package.[44] Beyond this, we also performed single-point computations at the EOM-CCSD(T)/cc-PVTZ level.[44] To reveal the adiabatic decomposition mechanisms of CHF_3^+ in the X^2A_1 and A^2A_2 states, their one-dimensional H-loss and F-loss potential energy surfaces were mapped using time-dependent DFT (TD-DFT) at the UB3LYP/6-311+G(d,p) level. As described previously,[39,40] at every given C–H or C–F distance, the other geometrical parameters were re-optimized to verify the local minima. Moreover, the VIE values were defined as the energy difference between the ground-state neutral molecule and the excited ionic states, both at the optimized geometry of neutral CHF_3, while the AIEs were computed as the energy difference between the neutral molecule and the cation, each with its own optimized geometry. All calculations were performed using the Gaussian 16 program package.[44]

Using the optimized geometries, harmonic frequencies, and normal-mode vectors for each electronic state, the FC factors (FCFs) were calculated as the overlaps between the initial and target vibrational states in the harmonic approximation using the ezSpectrum program.[45] Full widths at half-maximum (FWHMs) of 500 and 30 meV were used for the X^2A_1 and C^2E states, respectively, in the simulated spectra and compared with the experimental spectra.

3. Results and discussions

3.1 Optimized geometries and ionization energies

Fig. 1 shows the optimized geometries of the neutral CHF_3 molecule and the CHF_3^+ cation. At the (U)B3LYP/6-311G+(d,p) level, the C–H bond length is significantly elongated from 1.090 Å in the neutral molecule to 1.321 Å in the cation, while the C–F bond slightly shrinks from 1.344 Å to 1.284 Å. This is consistent with the weakening of the C–H bond upon the production of the CHF_3^+ ions in their electronic ground state owing to the removal of an electron from the σ_{C-H} orbital of neutral CHF_3. Although a stable structure in the ground state was predicted by theoretical calculations, no such CHF_3^+ ions were detected in ionization experiments. Because the C–H bond of CHF_3^+ is much longer than that of neutral CHF_3, the local minimum on the ion potential energy surface is far away from the FC region, resulting in a higher internal energy of CHF_3^+ after FC ionization than the dissociation limit. Consequently, the rapid dissociation of these ions populating the lowest dissociation limits may result in a lack of detection of this parent ion in the mass spectra.[19]

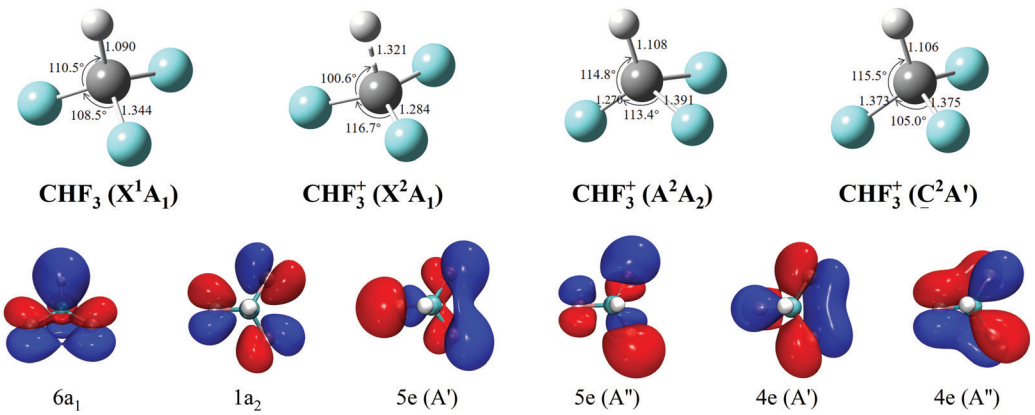

Fig. 1 Optimized geometries and outer molecular orbitals of the neutral CHF_3 molecule and the CHF_3^+ cation at the (U)B3LYP/6-311G+(d,p) level.

 This journal is © the Owner Societies 2020

At the EOM-CCSD(T)/cc-PVTZ//B3LYP/6-311G+(d,p) level, we computed AIE (CHF_3) = 13.86 eV, which accords well with previously reported data (14.03 eV,[7] 13.82 eV,[6] and 13.86 eV[18]). Indeed, since the equilibrium geometries of the neutral and ionic species are relatively different, especially for the C–H bond, we expect an unfavorable FC factor for such a transition. Moreover, the VIE for this transition should be considerably larger than the AIE. This is in line with the present EOM-CCSD(T)/cc-pVTZ computations, which give a VIE of 15.04 eV. A 1.18 eV energy gap between VIE and AIE strongly confirms a significant geometry change upon photoionization.

Along the C–F bond rupture, the molecular symmetry of CHF_3^+ evolves from C_{3v} to C_s, thus, each doubly degenerate state, such as B^2E and C^2E, will split into two components with $^2A'$ and $^2A''$ spatial symmetry, implying that there are five excited states involved in the energy range. Only optimized geometries of the A^2A_2 and C^2A' states were successfully obtained, as shown in Fig. 1, while the others failed owing to non-converging wavefunctions in the TD-UB3LYP calculations. Compared with the ground ionic state X^2A_1, CHF_3^+ has a shorter C–H bond length in both excited states, which indicates the bound feature along the C–H coordinate for these two states. This inference also agrees with the characteristics of the $1a_2$ and 4e orbitals (in Fig. 1). Using these optimized geometries, the AIE values for the excited states were calculated at the EOM-CCSD(T)/cc-PVTZ level (listed in Table 1 for comparison), *e.g.*, 15.09 eV for A^2A_2 and 17.23 eV for C^2A'. A large energy gap (0.66 eV) between AIE and VIE for the A^2A_2 state indicates that there is a considerable geometric change upon photoionization, whereas the close AIE and VIE values of C^2A' imply a geometry similar to that of the neutral molecule.

As listed in Table 1, the calculated VIE values for the X^2A_1, A^2A_2, B^2E, and C^2E states at the EOM-CCSD(T)/cc-PVTZ level are 15.04, 15.75, 16.29, and 17.29 eV, respectively, which agree with the previous experimental data.[8,18,19] The consistent results indicate that the single-reference TD-UB3LYP method is economical and can be applied to map the potential energy surfaces of these states, as described in Section 3.5.

3.2 Threshold photoelectron spectrum

Fig. 2 shows the recorded TPES of CHF_3 in the energy range of 13.90–18.00 eV, with a step size of 5 meV, which has been normalized by dividing the TPE intensity by the experimentally measured photocurrent. According to previous studies,[8,19] the first two structureless bands are contributed by three electronic states of CHF_3^+, *i.e.*, X^2A_1, A^2A_2, and B^2E, while the third one with a series of discernible vibrational peaks is assigned to C^2E. Moreover, the second peak looks like the sum of a low-energy shoulder at ~15.6 eV and an intense band at ~15.9 eV. Both sub-bands were also observed in Parkes *et al.*'s TPES;[19] however, they showed the opposite intensity ratios to our results. This difference may be caused by the auto-ionization of Rydberg states, which was efficiently suppressed in our measurement using special designs of the repelling electric field and electron detectors.[27] Notably, the calculated transition factor for the ionizations to the A^2A_2 state was much lower than that for B^2E. Thus, in our work, the weak band at the low-energy side was assigned to the A^2A_2 state, while the strong band with a peak at ~15.9 eV was mainly attributed to B^2E. Hence, the VIE for the B^2E state was determined to be 15.92 eV in the present work, rather than approaching 16.35 eV, as suggested by Parkes *et al.*,[19] which is located on the right shoulder of our B^2E band. The splitting due to symmetry-breaking in the C–F bond rupture further complicates the assignment of the band. Moreover, the experimental VIE values for the X^2A_1, A^2A_2, B^2E, and C^2E states were derived from TPES to be 14.64, 15.59, 15.92, and 17.24 eV, respectively, which were in general agreement with the previous data.[8,19]

For the X^2A_1 state, FC factor simulation was performed using the ezSpectrum program[45] based on the calculated geometry and frequencies, as shown by the left red line in Fig. 2. According to the rising edge of the TPES, AIE = 13.67 eV could be determined. This value is smaller than the previously reported data (14.03,[7] 13.82,[6] and 13.86 eV[18]) and our calculated value (13.86 eV). Apparently, the value of AIE = 13.67 eV from the FC simulation is sufficiently reliable, and the large difference between the AIE and VIE values indicates that there is a considerable geometric change in CHF_3 upon ionization. Moreover, the C–H stretching vibration (ν_9, 1375 cm^{-1}) mode is predominantly excited upon ionization, as suggested by the FC simulation, which agrees with the primary geometry change from a neutral molecule to a cation in Fig. 1. The large FWHM of 0.5 eV in the simulation is consistent with the dissociative property of X^2A_1.

For the C^2E state of CHF_3^+, a series of vibrational peaks superimposed on a wide background were clearly distinguished in the magnified TPES (Fig. 2). Notably, the vibrational structure was indiscernible in previous TPES[19] owing to a very strong background. This background may have arisen through the

Table 1 Vertical (VIEs) and adiabatic (AIEs) ionization energies of CHF_3, as well as their difference (ΔE)

	VIE (eV)		AIE (eV)		ΔE (eV)	
States	Expt.	Calc.	Expt.	Calc.	Expt.	Calc.
X^2A_1	14.64,[a] 14.80,[b] 14.77,[c] 14.81[d]	15.04[e]	13.67,[a] 13.86[c]	13.86,[e] 13.82,[f] 14.03[g]	0.97	1.18
A^2A_2	15.59,[a] 15.5,[b] 15.46,[c] 15.57[d]	15.75[e]	—	15.09[e]	—	0.66
B^2E	15.92,[a] 16.2,[b] 16.16,[c] 16.35[d]	16.29[e]	—	—	—	—
C^2E	17.24,[a] 17.24,[b] 17.26,[c] 17.28[d]	17.29[e]	17.11[a]	17.23[e]	0.13	0.06

[a] The present TPES results, in which the AIEs were obtained from spectral simulations. [b] From ref. 8. [c] From ref. 18. [d] From ref. 19. [e] Calculated at the EOM-CCSD(T)/cc-PVTZ level using the UB3LYP/6-311+G(d,p) optimized CHF_3 geometry. [f] Calculated at the B3LYP/6-31G(2df,p) level using the G3X model from ref. 6. [g] Calculated at the MP2/6-31G(d) level using the G3 procedure from ref. 7.

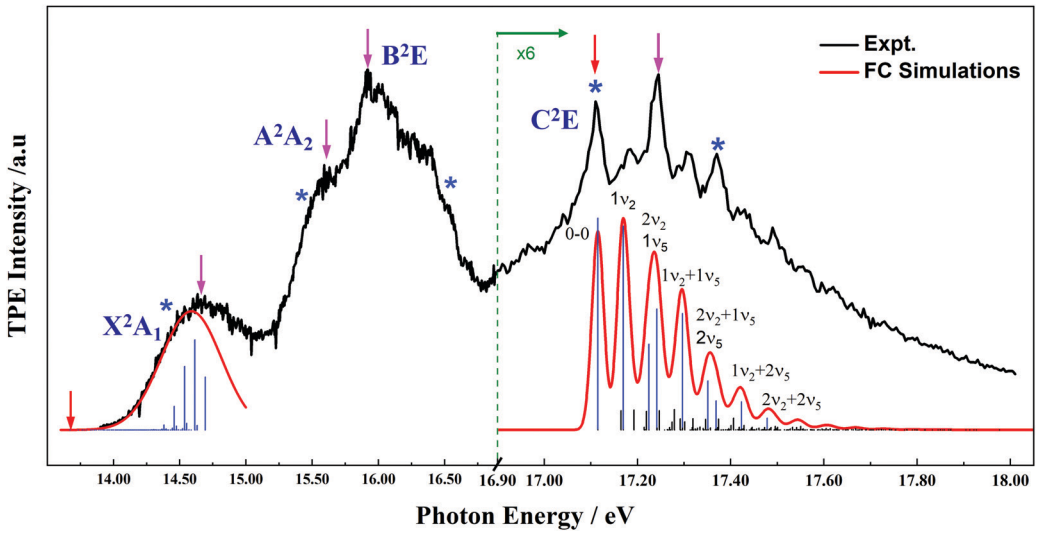

Fig. 2 Threshold photoelectron spectra (TPES, black line) of CHF_3 in the photon energy range of 13.90–18.00 eV, together with the FC-simulated spectra (red lines) of the X^2A_1 and C^2E bands, where the vertical blue lines represent the FC-simulated ionization transitions. The red and magenta arrows point to the AIEs and VIEs of the low-lying electronic states, respectively, and the coincident TOF mass spectra were recorded at the energies marked with blue stars.

auto-ionization of Rydberg states, which was also suppressed in the present measurements. A similar vibrational structure was also dimly observed in the He-I photoelectron spectrum.[8] An FC factor simulation was performed using the ezSpectrum program[45] (Fig. 2). The simulated spectrum with a 30 meV FWHM is generally consistent with the experimental result. As suggested by the simulation, the resolved vibrational structure was dominated by the excitation of two C–F symmetric deformation (ν_2, 565 cm^{-1}) and symmetric stretching (ν_5, 1049 cm^{-1}) vibrational modes. Based on the assignment, the AIE and VIE values for C^2A' were easily determined by experiment to be 17.11 and 17.17 eV, respectively.

3.3 TPEPICO-TOF mass spectra

Fig. 3 shows the TPEPICO-TOF mass spectra at several specific photon energies, *e.g.*, 14.39 (for X^2A_1), 15.41 (for A^2A_2), 15.93 and 16.56 (for B^2E), and 17.12 and 17.38 eV (for C^2E). No parent ions were observed at all photon energies (expected to appear at t = 17.18 μs). The first fragment ion, CF_3^+, was clearly observed from the C–H bond cleavage at 17.08 μs for the X^2A_1 state, but it quickly disappeared when the photon energy reached the A^2A_2 state. Its triangle-like TOF profile strongly implied a statistical dissociation along the C–H bond rupture. At the representative energy of A^2A_2 (15.41 eV), the predominant fragment ions became CHF_2^+, as yielded by C–F bond breaking, while only a small number of CF_3^+ ions were residual with a fraction of ~3%. The present branching ratio of the C–H and C–F bond cleavages was much different from Parkes *et al.*'s measurement,[19] in which the branching ratio of CHF_2^+ and CF_3^+ was reported to be 0.68 : 0.32 at a similar energy level (15.58 eV). As with the above discussion of TPES, this difference may arise from the contribution of auto-ionization of the 5e → 10a_1 Rydberg states in the FC gap between X^2A_1 and A^2A_2.[46] The present branching ratios were verified with high confidence.

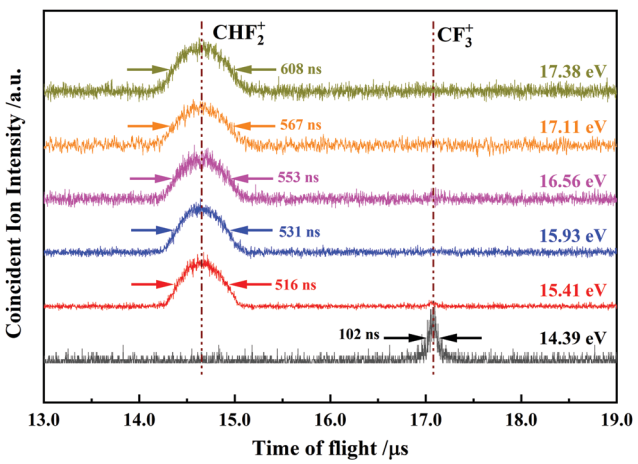

Fig. 3 TPEPICO time-of-flight mass spectra at $h\nu$ = 14.39, 15.41, 15.93, 16.56, 17.11, and 17.38 eV.

Notably, the CHF_2^+ TOF profile with a flat top was entirely different from that of CF_3^+. The greater than 500 ns FWHM of the CHF_2^+ peak indicates that a lot of excess energy was released to translational degrees of freedom during C–F bond cleavage. Its profile was wide enough (~800 ns) to apply a mass gate of ~40 ns for time-sliced velocity imaging. Moreover, as shown in Fig. 3, the width of CHF_2^+ slightly increased with photon energy over the entire range of the A^2A_2, B^2E, and C^2E states, indicating that for highly excited states like B^2E and C^2E, more excess energies are distributed in other internal degrees of freedom rather than the translational energy release when the C–F bond is broken.

3.4 C–H bond breaking mechanism of CHF_3^+ in the X^2A_1 state

In the experiment, the statistical decomposition mechanism of the triangle-like TOF profile of CF_3^+ was verified. To further reveal the initial dissociative behavior of CHF_3^+ ions upon

 This journal is © the Owner Societies 2020

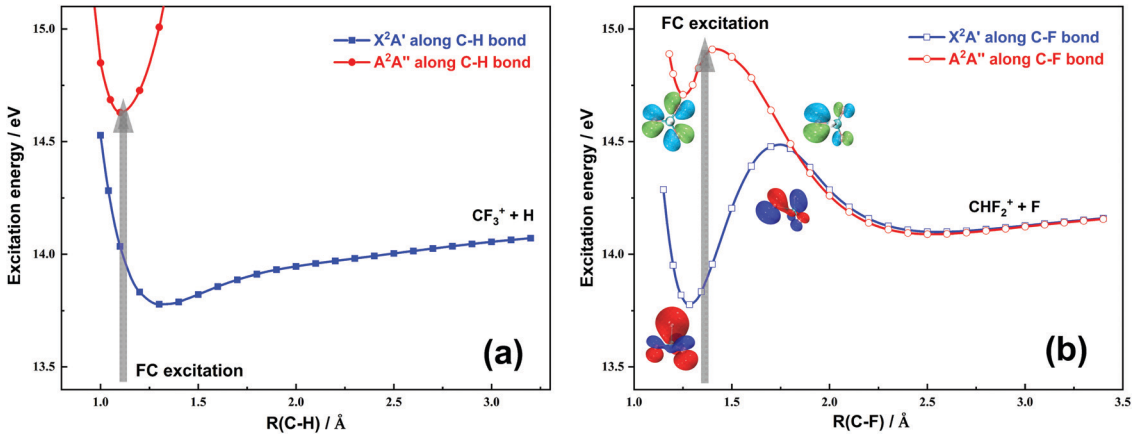

Fig. 4 TD-UB3LYP/6-311G+(d,p) potential energy curves of CHF_3^+ in the X^2A_1 and A^2A_2 states along (a) C–H bond cleavage and (b) C–F bond cleavage. The predominant electron-detached molecular orbitals at specific C–F distances are also shown. The thick gray arrows indicate the FC regions of photoionization along the C–F and C–H coordinates, respectively.

FC ionization, the adiabatic excited potential energy curves along the C–H coordinate were calculated at the UB3LYP/6-311G+(d,p) level (Fig. 4(a)), in which the other geometric parameters, except the C–H distance, were optimized at their minimum energy values. The X^2A_1 state of CHF_3^+ along the C–H bond is apparently bound, which implies that the statistical dissociation mechanism of the experimentally observed H-loss pathway is reasonable. The TPEPICO-TOF mass spectra indicate that a CF_3^+ fragment ion was only produced in the X^2A_1 state of CHF_3^+, so we can guess that the excited states of A^2A_2, B^2E, and C^2E are bound along the C–H bond. This is confirmed by the calculated potential energy curve of A^2A_2 in Fig. 4(a). Additionally, to further understand the dissociative properties of $CHF_3^+(X^2A_1)$, the adiabatic potential energy curve of $CHF_3^+(X^2A_1)$ along the C–F coordinate was also calculated (Fig. 4(b)). The X^2A_1 state is bound in the FC region, irrespective of the C–F and C–H bond ruptures, which is analogous to the A^2A_1 state of CF_3Cl^+ owing to their similar HOMO of a_1 symmetry essentially contributed by the $\sigma_{C-H/Cl}$ bonds.[39,40] By contrast, the barrier for breaking the C–H bond is much lower than that for C–F bond cleavage. Moreover, the single-point energy calculation of the H-loss products (CF_3^+ + H) and $CHF_3^+(X^2A_1)$ at the EOM-CCSD(T)/cc-PVTZ level suggests that the corresponding decomposition of $CHF_3^+(X^2A_1) \rightarrow CF_3^+(X^1A_1) + H(^2S)$ is slightly exothermic. Evidently, the $CHF_3^+(X^2A_1)$ ions predominantly dissociate to produce CF_3^+ (rather than CHF_2^+) in nature.

3.5 TPEPICO images of CHF_2^+ fragment ions in the A_2A_2 and B^2E states

As mentioned above, accurate KERDs and angular distributions are necessary to understand non-statistical dissociation dynamics. Thus, using a mass gate of 40 ns for the CHF_2^+ fragment ion, the three-dimensional time-sliced TPEPICO velocity map images of CHF_2^+ were measured. Three specific photon energies were selected: 15.41 eV for A^2A_2 and 15.92 and 16.56 eV for B^2E. Fig. 5 shows the recorded images, in which the electric vector ε of the VUV photons is vertical. The three images have very similar patterns; each includes a bright, anisotropic ring together with a weak central spot, which in general indicates a dominantly non-statistical bond-breaking channel and a statistical decomposition pathway.

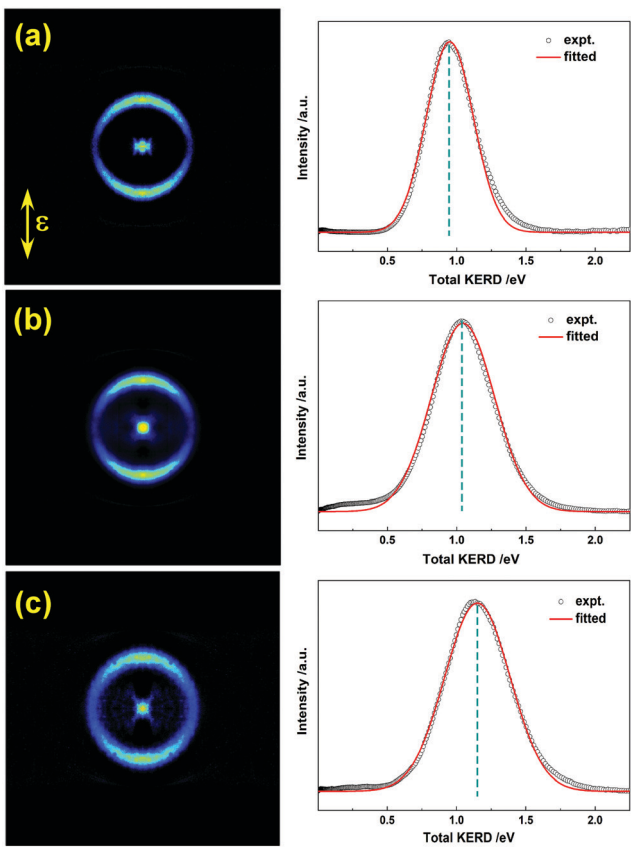

Fig. 5 Time-sliced TPEPICO velocity map images of CHF_2^+ at 15.41 (a), 15.93 (b), and 16.56 eV (c), as well as the corresponding total kinetic energy released distributions (KERDs).

By accumulating angular image intensity, the speed distribution of CHF_2^+ was obtained. Based on the conservations of linear momentum and energy, the total KERD of the decomposition channel was then determined, as shown in the right panel

of Fig. 5. Apparently, the fraction of the central spot in the total ion count is too low (~2%) to be observed in the mass spectra. Its occurrence can be easily attributed to internal conversion to X^2A_1, followed by statistical C–F bond cleavage. Although we do not pay more attention to this statistical pathway because its branching ratio is too small, its existence provides definite evidence that neither A^2A_2 nor B^2E are repulsive, as inferred from previous studies.[19,21] Generally, the outer anisotropic ring in images with a predominant portion implies repulsive characteristics with a relatively large kinetic energy release. At the three photon energies, all total KERD curves in Fig. 5 could be fitted well with a Gaussian-type profile, verifying the non-statistical F-loss dynamics of CHF_3^+ in the A^2A_2 and B^2E states. These results agree well with the previous study of Parkes *et al.*[19]

As shown in Fig. 5, the average total kinetic energy release during the C–F bond cleavage, ⟨TKE⟩, was slightly increased as the photon energy increased from A^2A_2 to B^2E, *e.g.*, 0.95 eV at 15.41 eV (A^2A_2), 1.04 eV at 15.93 eV, and 1.15 eV at 16.56 eV for B^2E, respectively. For a DPI process to break the C–F bond, excess energy (E_{excess}) can be calculated as $E_{excess} = h\nu - \Delta_rH_{0K}(CHF_3 \rightarrow F + CHF_2^+ + e)$, where the formation enthalpy of the $F + CHF_2^+$ channel, Δ_rH_{0K}, is 14.18 eV.[25,26] Because E_{excess} could be distributed to the fragments' translational and internal energy based on energy conservation, the ratio of ⟨TKE⟩ to E_{excess} was calculated (f_T = ⟨TKE⟩/E_{excess}) to be 0.77, 0.59, and 0.48 (Table 2). The classical impulsive model[47] is usually utilized to describe the direct dissociation along a repulsive potential energy surface in which a molecule rapidly decomposes along a simple diatomic vibrational coordinate, whereas other atoms play spectator roles. Consequently, the dissociating fragments ($F + CHF_2^+$) recoil sharply and release repulsive potential energy at a short bond length, whereas the other degrees of freedom scarcely change. Thus, the TKE of both fragments is related to the excess energy E_{excess}, and the f_T value is calculated to be μ_{C-F}/μ_{CHF_2-F} = 0.53, where μ_{C-F} and μ_{CHF_2-F} are the reduced masses of carbon and fluorine atoms and the CHF_2 moiety and the fluorine atom, respectively.

At 15.93 and 16.56 eV in the B^2E state, the experimental $\langle f_T \rangle$ values in Table 2 are close to the impulsive limit. Thus, a repulsive F-loss mechanism similar to previous conclusions[19] can be confidently suggested for the dissociation of $CHF_3^+(B^2E)$. As mentioned above, the B^2E state of CHF_3^+ has a valence bond electronic configuration similar to that of CF_3Cl^+ in the C^2E state. Considering the bound property of $CF_3Cl^+(C^2E)$ along the C–F coordinate,[40] we deduce that the B^2E state of CHF_3^+ may also be bound along the C–F coordinate. Thus, the dissociation of $CHF_3^+(B^2E)$ may occur *via* coupling to a lower repulsive state by internal conversion prior to rapid decomposition along the C–F bond. To our surprise, the experimental $\langle f_T \rangle$ value of A^2A_2 was 0.77 at 15.41 eV, which was higher than the impulsive limit. In the classical impulsive model, CHF_2^+ plays a spectator role when the fluorine atom and CHF_2^+ recoil sharply and separate in a short time; the internal energy redistribution of CHF_2^+ then proceeds from its initial recoiled kinetic energy, resulting in a maximal $\langle f_T \rangle$ value of μ_{C-F}/μ_{CHF_2-F}. By contrast, more excess energies distributed in the translational degrees of freedom observed at 15.41 eV indicate that the decomposition of $CHF_3^+(A^2A_2)$ occurs at a relatively faster rate than that for B^2E or the dynamic impulsive limit.

From the images in Fig. 5, the angular distributions of the CHF_2^+ fragment ions were also obtained by integrating the image intensity over an appropriate range of speeds at each angle. Then, the anisotropy parameters β at the specific energies were derived by fitting the angular distributions,[48] they are summarized in Table 2. For the dominant decomposition channel corresponding to the outer ring in the images, the β values were 0.86 ± 0.01 at 15.41 eV, 0.83 ± 0.01 at 15.93 eV, and 0.72 ± 0.02 at 16.56 eV. Apparently, these values are close to 1, indicating that both the A^2A_2 and B^2E states have a trend of fast parallel dissociation; moreover, their lifetimes are less than the rotational period of the molecular ion.

To further reveal interactions in the region far from FC ionization, the adiabatic potential energy curves of CHF_3^+ in the X^2A_1 and A^2A_2 states along C–F bond cleavage were calculated at the TD-UB3LYP/6-311G+(d,p) level (Fig. 4(b)). The A^2A_2 state is predissociative along the C–F coordinate. However, considering the overestimated barrier height at the TD-UB3LYP level,[39,40] the initial energy of a $CHF_3^+(A^2A_2)$ ion upon FC ionization may exceed the barrier, resulting in direct dissociation along the repulsive C–F coordinate. Notably, the dynamic behavior of $CHF_3^+(A^2A_2)$ along the C–F coordinate differs from that of $CF_3Cl^+(B^2A_2)$ as a typical bound state, although they have similar electron-detached molecular orbitals contributed by the 2pπ orbitals of the fluorine atom. Apparently, this decomposition rate of A^2A_2 is faster than that of B^2E occurring through internal conversion. This agrees with the changes in the experimental β values in Table 2.

In addition, analyses of the natural bond orbital (NBO)[49] reveal the changes in the molecular orbitals along the C–F bond cleavage in Fig. 4(b). As mentioned above, the electron that is removed to form the $CHF_3^+(X^2A_1)$ ion is predominantly detached from the HOMO with $6a_1$ symmetry. However, with an increase in the C–F distance, the major electronic configuration of X^2A_1 changes, and a more significant contribution from the 2pπ orbital of the dissociating fluorine atom is found from ~1.7 Å onwards. Because the 2pπ orbital of the fluorine atom is a major contributor to the HOMO−2 with 5e symmetry, this change in electronic configuration further confirms the existence of a strong coupling between the X^2A_1 and B^2E states. Under the restrictions of C_s symmetry, the $^2A'$ state split from B^2E should be the chief

Table 2 Average total kinetic energy release ⟨TKE⟩, excess energy E_{excess}, and anisotropy parameter β of the C–F bond cleavage of CHF_3^+ in various excited electronic states

State	$h\nu$/eV	⟨TKE⟩/eV	E_{excess}[a]/eV	f_T	β
A^2A_2	15.41	0.95	1.23	0.77	0.86 ± 0.01
B^2E	15.93	1.04	1.75	0.59	0.83 ± 0.01
	16.56	1.15	2.38	0.48	0.72 ± 0.02
C^2E	17.12	1.08	2.94	0.37	0.26 ± 0.02
	17.38	1.06	3.20	0.33	0.28 ± 0.02

[a] $E_{excess} = h\nu - \Delta_rH_{0K}(CHF_3 \rightarrow F + CHF_2^+ + e)$.

This journal is © the Owner Societies 2020

state causing the predissociative barrier owing to avoided crossing between X^2A' and B^2A'. In fact, very similar interactions have been reported in the dissociation of $CF_3Cl^+(A^2A_1)$.[40] To further clarify the interaction between the X^2A_1 and B^2A' states, a multi-reference configuration interaction calculation is being performed.

For the A^2A_2 state of CHF_3^+, the dominant electronic configuration remains, and only the component coefficients of three F(2pπ) orbitals exhibit moderate changes. As shown in Fig. 4(b), the ionized electron is predominantly detached from HOMO−1 with $1a_2$ symmetry, regardless of whether it is in the FC region or at a larger C–F distance. Interestingly, a similar phenomenon was also observed for the B^2A_2 state of CF_3Cl^+ with an unchanged major electronic configuration;[40] however, the latter was typically bound along the C–F coordinate. Thus, the entirely different performances for $CHF_3^+(A^2A_2)$ and $CF_3Cl^+(B^2A_2)$ indicate a significant substitutional effect of the chlorine atom on C–F binding. The repulsive force of the 3pπ electrons of the chlorine atom may hinder changes in the F(2pπ) orbital coefficients.

3.6 TPEPICO image of the CHF_2^+ fragment ions in the C^2E state

The discernible vibrational structure of the C^2E band in TPES indicates its bound feature along both the C–H and C–F bonds, although only CHF_2^+ fragment ions were observed in the mass spectra. Because the adiabatic F-loss limit of the C^2E state is too high to attain in this experiment, the observed decomposition of $CHF_3^+(C^2E)$ must proceed through internal conversion, followed by rapid repulsive dissociation. Two photon energies of 17.12 and 17.38 eV were selected to investigate the vibrational excitation effect on total KERD in the F-loss dynamics of $CHF_3^+(C^2E)$. Fig. 6 shows the TPEPICO velocity images of the CHF_2^+ fragment ions at these two energies. The image patterns are very similar to those in Fig. 5 for the A^2A_2 and B^2E states. Besides a central spot with a limited fraction, an outer ring corresponding to fast dissociation is dominant. The total KERD curves also fitted very well with a Gaussian-type profile, indicating the rapid dissociation characteristics of the C^2E state, as revealed in previous experiments.[19]

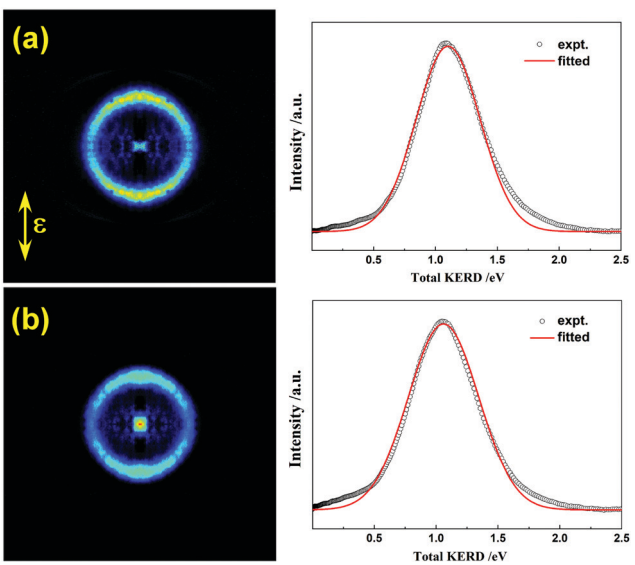

Fig. 6 Time-sliced TPEPICO velocity map images of CHF_2^+ at 17.12 (a) and 17.38 eV (b), as well as the corresponding total KERDs.

According to the TPES assignment in Fig. 2, the vibration excitation predominantly corresponds to the symmetric stretching of two other C–F bonds (ν_5). Surprisingly, the average total kinetic energy release was almost unchanged with vibrational excitation (*i.e.*, $\langle TKE \rangle$ = 1.08 eV at 17.12 eV and 1.06 eV at 17.38 eV). Moreover, the $\langle TKE \rangle$ value of C^2E was even slightly reduced in comparison with the dynamics of the B^2E state in Table 2, although the internal energy of the parent ion was increased by more than 0.5 eV. Accordingly, the $\langle f_T \rangle$ values were 0.37 at 17.12 eV and 0.33 at 17.38 eV, respectively, which were apparently lower than the impulsive limit. These $\langle f_T \rangle$ data also agree very well with the previous TPEPICO measurements.[19] In addition, the anisotropy parameter β was measured to be 0.26 (17.12 eV) and 0.28 (17.38 eV), indicating parallel dissociation. Compared with the cases of the A^2A_2 and B^2E states, the lower β values also imply a slower dissociation rate of C^2E along the F-loss pathway; thus, more excess energy is trapped within the internal energy of the fragment prior to repulsive dissociation. Similar dynamic behaviors were observed in the F-loss dissociation of $CF_3Cl^+(D^2E)$[39] and the C–F bond rupture of $CF_4^+(B^2E)$.[20]

4. Conclusions

Dissociative photoionization of CHF_3 in the 13.90–18.00 eV energy range was investigated by TPEPICO imaging using synchrotron radiation VUV photoionization. TPES included the contributions of four low-lying electronic states of CHF_3^+, *i.e.*, X^2A_1, A^2A_2, B^2E, and C^2E. Only the C^2E band showed a discernible vibrational structure, and FC simulations provided the vibrational assignment in which the excitation of the C–F symmetric deformation (ν_2, 565 cm^{-1}) and symmetric stretching (ν_5, 1049 cm^{-1}) was confirmed. Based on the spectral assignment and high-level ionization energy calculations, the AIE and VIE values of the electronic states of CHF_3^+ were reliably determined.

In the coincident mass spectra, a unique CF_3^+ fragment ion was observed for $CHF_3^+(X^2A_1)$ ions, while C–F bond breaking in CHF_3^+ in the A^2A_2, B^2E, and C^2E states was verified to produce CHF_2^+ fragment ions. To clarify the dissociation mechanism of CHF_3^+ in low-lying excited states such as A^2A_2, B^2E, and C^2E, the time-sliced TPEPICO velocity map images of the CHF_2^+ fragment ions were recorded at several specific photon energies, *i.e.*, 15.41 eV for A^2A_2, 15.92 and 16.56 eV for B^2E, and 17.12 and 17.38 eV for C^2E. In all images, identical patterns were observed as a bright, anisotropic ring with a weak central spot. A statistical dissociation mechanism *via* internal conversion followed by statistical decomposition along the C–F bond is assumed to contribute the central component. However, it was mostly ignored because it was only a minor channel. For the dominant anisotropic ring component, the total KERD curve can be fitted well with a Gaussian-type profile indicating rapid repulsive dissociation. Moreover, the $\langle f_T \rangle$ values decreased with photon

energy from A^2A_2 to C^2E. A similar trend was observed for the anisotropic parameter β. Thus, more excess energy remains in the internal energy of the CHF_2^+ fragment ion in the higher excited states owing to their slower decomposition rates.

With the aid of the potential energy curves of CHF_3^+ along both the C–H and C–F bond cleavages, the dissociation mechanisms of the X^2A_1, A^2A_2, B^2E, and C^2E states can be revealed from the experimentally measured KERDs and angular distributions. The C–H bond breaking of $CHF_3^+(X^2A_1)$ undoubtedly follows a statistical dissociation mechanism. Because the internal energy of the parent ion is higher than the $CF_3^+(X^1A_1) + H(^2S)$ dissociation limit upon FC ionization, $CHF_3^+(X^2A_1)$ ions predominantly dissociate to produce CF_3^+ rather than CHF_2^+ owing to the repulsive C–F bond cleavage. $CHF_3^+(A^2A_2)$ ions can directly decompose along the repulsive F-loss potential energy surface upon formation. The dissociation rate was verified to be faster than the impulsive limit. By contrast, the F-loss dynamics of the B^2E and C^2E states become much more complicated. The bright central spot in the images indicates a previously unobserved internal conversion pathway, followed by statistical dissociation on the X^2A_1 potential energy surface. The predominant outer ring in the images is explained by non-statistical dissociation. For the bound states along the C–F coordinate, a two-step decomposition mechanism of $CHF_3^+(B^2E$ and $C^2E)$ can be deduced as internal conversion to the lower repulsive A^2A_2 state, followed by adiabatically fast dissociation. Additionally, with the change from C_{3v} to C_s symmetry during the F-loss process, the ^2E state splits into $^2A'$ and $^2A''$ substates. Under the C_s symmetry restriction, the $^2A'$ state split from B^2E should be the main state causing the predissociative barrier owing to the crossing between X^2A' and B^2A' being avoided.

Conflicts of interest

There are no conflicts of interest to declare.

Acknowledgements

The authors sincerely appreciate Prof. Majdi Hochlaf for his fruitful discussions and help in English writing. The work was financially supported by the National Key Research and Development program of China (No. 2016YFF0200502), and the National Natural Science Foundation of China (No. 21903079, 21573210 and 21873089). X. Zhou also thanks the USTC-NSRL Association for funding support.

References

1 M. Baasandorj, B. D. Hall and J. B. Burkholder, *Atmos. Chem. Phys.*, 2012, **12**, 11753–11764.
2 P. H. Yih, V. Saxena and A. J. Steckl, *Phys. Stat. Sol.*, 1997, **202**, 605–642.
3 M. Belotti, M. Galli, D. Bajoni, L. C. Andreani, G. Guizzetti, D. Decanini and Y. Chen, *Microelectron. Eng.*, 2004, **73–74**, 405–411.
4 G. S. Oehrlein, Y. Zhang, D. Vender and O. Joubert, *J. Vac. Sci. Technol., A*, 1994, **12**, 333–344.
5 F. S. Rowland and M. J. Molina, *Rev. Geophys.*, 1975, **13**, 1–35.
6 Y. L. He and L. M. Wang, *Struct. Chem.*, 2009, **20**, 461–479.
7 N. L. Ma, K.-C. Lau, S.-H. Chien and W.-K. Li, *Chem. Phys. Lett.*, 1999, **311**, 275–280.
8 C. R. Brundle, M. B. Robin and H. Basch, *J. Chem. Phys.*, 1970, **53**, 2196–2213.
9 A. W. Potts, H. J. Lempka, D. G. Streets and W. C. Price, *Phil. Trans. Roy. Soc. Lond. A*, 1970, **268**, 59–76.
10 A. Amrein, M. Quack and U. Schmitt, *J. Phys. Chem.*, 1988, **92**, 5455–5466.
11 J. C. Creasey, I. R. Lambert, R. P. Tuckett and A. Hopkirk, *Mol. Phys.*, 1990, **71**, 1355–1366.
12 L. G. Christophorou and J. K. Olthoff, *J. Phys. Chem. Ref. Data*, 1999, **28**, 967–982.
13 J. E. Baio, H. Yu, D. W. Flaherty, H. F. Winters and D. B. Graves, *J. Phys. D: Appl. Phys.*, 2007, **40**, 6969–6974.
14 L. G. Christophorou, J. K. Olthoff and M. Rao, *J. Phys. Chem. Ref. Data*, 1997, **26**, 1–15.
15 S. Motlagh and J. H. Moore, *J. Chem. Phys.*, 1998, **109**, 432–438.
16 J. Jankunas, K. Jachymski, M. Hapka and A. Osterwalder, *J. Chem. Phys.*, 2016, **144**, 221102.
17 B. L. Peko, R. L. Champion, M. Rao and J. K. Olthoff, *J. Appl. Phys.*, 2002, **92**, 1657–1662.
18 B. P. Pullen, T. A. Carlson, W. E. Moddeman, G. K. Schweitzer, W. E. Bull and F. A. Grimm, *J. Chem. Phys.*, 1970, **53**, 768–782.
19 M. A. Parkes, R. Y. L. Chim, C. A. Mayhew, V. A. Mikhailov and R. P. Tuckett, *Mol. Phys.*, 2006, **104**, 263–272.
20 X. Tang, X. Zhou, M. Wu, Z. Gao, S. Liu, F. Liu, X. Shan and L. Sheng, *J. Chem. Phys.*, 2013, **138**, 094306.
21 I. Torres, R. Martinez and F. Castano, *J. Phys. B: At., Mol. Opt. Phys.*, 2002, **35**, 2423–2436.
22 T. Fiegele, G. Hanel, I. Torres, M. Lezius and T. D. Mark, *J. Phys. B: At., Mol. Opt. Phys.*, 2000, **33**, 4263–4283.
23 M. Goto, K. Nakamura, H. Toyoda and H. Sugai, *Jpn. J. Appl. Phys.*, 1994, **33**, 3602–3607.
24 C. Q. Jiao, R. Nagpal and P. D. Haaland, *Chem. Phys. Lett.*, 1997, **269**, 117–121.
25 B. Ruscic and D. H. Bross, Active Thermochemical Tables (ATcT) values based on ver. 1.122g of the Thermochemical Network, 2019, available at ATcT.anl.gov.
26 J. Harvey, R. P. Tuckett and A. Bodi, *J. Phys. Chem. A*, 2012, **116**, 9696–9705.
27 X. Tang, X. Zhou, M. Niu, S. Liu, J. Sun, X. Shan, F. Liu and L. Sheng, *Rev. Sci. Instrum.*, 2009, **80**, 113101.
28 A. Bodi, P. Hemberger, T. Gerber and B. Sztáray, *Rev. Sci. Instrum.*, 2012, **83**, 083105.
29 G. A. Garcia, B. K. C. D. Miranda, M. Tia, S. Daly and L. Nahon, *Rev. Sci. Instrum.*, 2013, **84**, 053112.
30 T. Baer and R. P. Tuckett, *Phys. Chem. Chem. Phys.*, 2017, **19**, 9698–9723.
31 X. Wu, X. Tang, X. Zhou and S. Liu, *Chin. J. Chem. Phys.*, 2019, 11–32.
32 C. Y. Ng, *Annu. Rev. Phys. Chem.*, 2002, **53**, 101–140.

 This journal is © the Owner Societies 2020

33 M. Steglich, V. B. F. Custodis, A. J. Trevitt, G. Dasilva, A. Bodi and P. Hemberger, *J. Am. Chem. Soc.*, 2017, **139**, 14348–14351.
34 K. Voronova, K. M. Ervin, K. G. Torma, P. Hemberger, A. Bodi, T. Gerber, D. L. Osborn and B. Sztáray, *J. Phys. Chem. Lett.*, 2018, **9**, 534–539.
35 A. Bodi, P. Hemberger, D. L. Osborn and B. Sztáray, *J. Phys. Chem. Lett.*, 2013, **4**, 2948–2952.
36 X. Tang, G. A. Garcia and L. Nahon, *J. Phys. Chem. A*, 2017, **121**, 5763–5772.
37 X. Tang, G. A. Garcia and L. Nahon, *Phys. Chem. Chem. Phys.*, 2015, **17**, 16858–16863.
38 X. Tang, G. A. Garcia and L. Nahon, *J. Phys. Chem. A*, 2015, **119**, 5942–5950.
39 X. Wu, G. Tang, H. Zhang, X. Zhou, S. Liu, F. Liu, L. Sheng and B. Yan, *Phys. Chem. Chem. Phys.*, 2018, **20**, 4917–4925.
40 X. Wu, T. Yu, Y. Chen, X. Zhou, S. Liu, X. Dai, F. Liu and L. Sheng, *Phys. Chem. Chem. Phys.*, 2019, **21**, 4998–5005.
41 X. Wu, M. Wu, X. Tang, X. Zhou, S. Liu, F. Liu and L. Sheng, *J. Phys. Chem. A*, 2017, **121**, 4743–4753.
42 B. Sztáray and T. Baer, *Rev. Sci. Instrum.*, 2003, **74**, 3763–3768.
43 A. Bodi, B. Sztáray, T. Baer, M. Johnson and T. Gerber, *Rev. Sci. Instrum.*, 2007, **78**, 084102.
44 M. J. Frisch, G. W. Trucks, H. B. Schlegel, G. E. Scuseria, M. A. Robb, J. R. Cheeseman, G. Scalmani, V. Barone and G. A. Petersson, *et al.*, *Gaussian 16 Revision C.01*, Gaussian, Inc., Wallingford CT, 2016.
45 V. A. Mozhayskiy and A. I. Krylov, *ezSpectrum, Version 3.0*, University of Southern California, Los Angeles, CA, http://Iopenshell.Usc.Edu/Downloads.
46 C. Larrieu, M. Chaillet and A. Dargelos, *J. Chem. Phys.*, 1991, **94**, 1327–1331.
47 K. E. Holdy, L. C. Klotz and K. R. Wilson, *J. Chem. Phys.*, 1970, **52**, 4588–4599.
48 R. N. Zare, *Mol. Photochem.*, 1972, **4**, 1–37.
49 T. Lu and F. Chen, *J. Comput. Chem.*, 2012, **33**, 580–592.